

## Fundamental aspects of terahertz near-field imaging and sensing

D.-S. KIM and Y.-M. BAHK, Seoul National University,  
Republic of Korea and P. C. M. PLANKEN,  
Delft University of Technology, The Netherlands

**DOI:** 10.1533/9780857096494.1.91

**Abstract:** The terahertz (THz) frequency range lies between optics and electronics, and THz frequencies are the lowest frequencies in which free space conventional optics can still be used before microwave components take over. Owing to its large wavelength, deep subwavelength phenomena of  $\lambda/100$  are experimentally accessible even with a few microns of spatial resolution. In this chapter, a number of different imaging techniques to overcome the diffraction limit in the THz frequency will be reviewed. Particular emphasis will be given to the giant field enhancements associated with sharp edges and antenna structures and how to estimate these field enhancements directly from imaging or from the diffraction formalism.

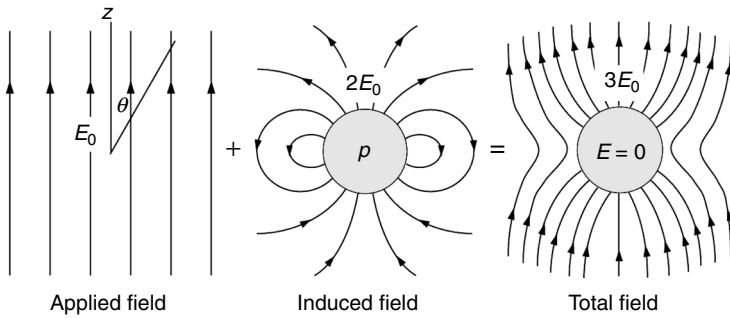
**Key words:** terahertz near-field measurement, terahertz spectroscopy, field enhancement, nanogap slot antenna, subwavelength optics.

### 4.1 Introduction

In this chapter, we proceed to discuss the properties of electromagnetic fields in the near- and far-field zones around a subwavelength object that serves as a source for the field. Near-field behavior with subwavelength distance from the source can have physical properties that are drastically different from the far-field. To understand the near-field behavior, we consider the simple system in which electric-dipole and magnetic-dipole are induced by the static ‘incident’ field. Furthermore, we examine the radiation of the induced electric- and magnetic-dipoles.

#### 4.1.1 Near-field and far-field

For the purpose of this chapter, it suffices to say that all near-field components are created by light impinging upon small, subwavelength objects. To illustrate this point, let us consider a static case applicable to the deep



4.1 Total enhanced electric field ( $E$ ) near a perfectly conducting sphere as a vector summation of the applied field,  $E_0$ , added to the electric field by the induced electric-dipole moment,  $p$ .

subwavelength regime: a perfectly conducting sphere of radius  $a$  placed in an initially uniform electric field  $E_0$ . This static field induces surface charge distribution with a dipole moment of  $p = 4\pi a^3 \epsilon_0 E_0$  which makes the inside-electric field zero, while creating a dipole field of

$$\vec{E} = \frac{1}{4\pi\epsilon_0} \frac{3(\hat{n} \cdot \vec{p})\hat{n} - \vec{p}}{r^3}$$

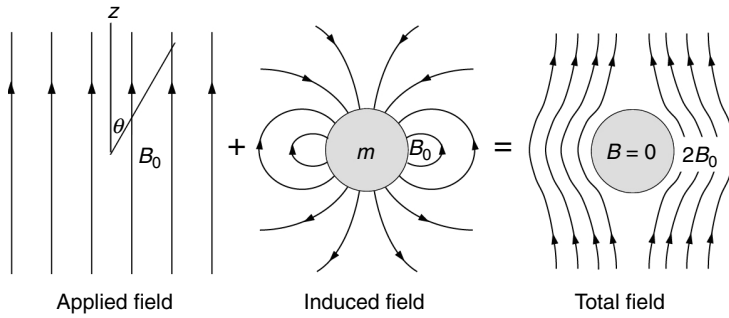
so that at the north and south poles, the induced field is twice that of the applied field. The sum of the applied field and the induced near-field gives rise to the total near-field  $3E_0$  found at the north and the south poles of the perfect electrical conductor (PEC) sphere (see Fig. 4.1):

$$\vec{E}_{\text{near}}(r = a; \theta = 0) = E_0 \hat{z} + \frac{1}{4\pi\epsilon_0} \frac{(3-1)4\pi\alpha^3 \epsilon_0}{\alpha^3} \hat{z} = E_0 \hat{z} + 2E_0 \hat{z} = 3E_0 \hat{z}.$$

For the magnetic field, in the optical regime, the magnetic-dipole moment  $m$  induced by the incident magnetic field  $B_0$  is much smaller than its electric-dipole counterpart:  $m \ll pc$  so that it is generally ignored. However, in the terahertz (THz) regime where the metals can be considered perfect in the quasi-static sense ( $\lambda \gg a \gg \delta$  (skin depth)), the magnetic-dipole effect can be comparable to that of the electric-dipole. To see this, we consider the effect of a time-varying magnetic field on a metallic sphere of radius  $a$ . The magnetic-dipole moment created by the induced currents should oppose the incident field inside the sphere. Knowing that the magnetic field of a magnetic dipole  $m$  is given by:

$$\vec{B} = \frac{\mu_0}{4\pi} \frac{3(\hat{n} \cdot \vec{m})\hat{n} - \vec{m}}{r^3},$$

Copyrighted Material downloaded from Woodhead Publishing Online  
 Delivered by http://www.woodheadpublishingonline.com  
 Young-Mi Bahk (153-83-420)  
 Sunday, November 24, 2013 10:08:06 PM  
 IP Address: 147.46.44.138



4.2 Total magnetic field ( $B$ ) distribution near a metallic sphere as a vector summation of the incident field,  $B_0$ , and the magnetic field by the induced magnetic-dipole moment,  $m$ .

we have the induced magnetic moment of  $m = -2\pi a^3(B_0/c)$  which will create a zero-field inside the sphere as well as at the north and south poles, while at the equator the incident and induced magnetic fields add to make the total field of  $2B_0$  (Fig. 4.2).

To summarize, the near-field is frequently associated with (1) new vector components non-existing on the incident field, and (2) a certain field enhancement.

#### 4.1.2 Radiation of the induced electric and magnetic-dipole moment

The induced electric-dipole creates electromagnetic fields of

$$\vec{H} = \frac{ck^2}{4\pi} (\hat{n} \times \vec{p}) \frac{e^{ikr}}{r} \left[ 1 - \frac{1}{ikr} \right] \tag{4.1}$$

$$\vec{E} = \frac{1}{4\pi\epsilon_0} \left\{ k^2 (\hat{n} \times \vec{p}) \times \hat{n} \frac{e^{ikr}}{r} + \left[ 3\hat{n}(\hat{n} \cdot \vec{p}) - \vec{p} \right] \left( \frac{1}{r^3} - \frac{ik}{r^2} \right) e^{ikr} \right\}, \tag{4.2}$$

where  $k$  is the wave vector and  $\hat{n}$  is a unit vector in the direction of the observation point.

We note that the magnetic field is transverse to the radial vector at all positions, but that the electric field has components both parallel and perpendicular to  $\hat{n}$ .

In the radiation zone ( $r \gg \lambda$ ), the fields can be written as

$$\vec{H}_{\text{far}} = \frac{ck^2}{4\pi} (\hat{n} \times \vec{p}) \frac{e^{ikr}}{r} \tag{4.3}$$

Copyrighted Material downloaded from Woodhead Publishing Online  
 Delivered by http://www.woodheadpublishingonline.com  
 Young-Mi Bahk (153-83-420)  
 Sunday, November 24, 2013 10:08:06 PM  
 IP Address: 147.46.44.138

$$\vec{E}_{\text{far}} = \frac{1}{4\pi\epsilon_0} \left\{ k^2 (\hat{n} \times \vec{p}) \times \hat{n} \frac{e^{ikr}}{r} \right\}. \quad [4.4]$$

In the near-field zone ( $r \ll \lambda$ ), on the other hand, induced fields take on the limiting forms,

$$\vec{H} = \frac{i\omega}{4\pi} (\hat{n} \times \vec{p}) \frac{1}{r^2} \quad [4.5]$$

$$\vec{E} = \frac{1}{4\pi\epsilon_0} \frac{3\hat{n}(\hat{n} \cdot \vec{p}) - \vec{p}}{r^3}. \quad [4.6]$$

It is interesting to note that the electric-dipole induced magnetic field is much weaker than the incident magnetic field at all distances: in the perfect conductor case, the induced magnetic field is at most  $(2\pi a/\lambda)H_0 \ll H_0$  even for  $r = a$ , in contrast to the induced electric field that can reach a maximum value of  $2E_0$  at the near-zone.

The magnetic field for an induced magnetic-dipole source is equal to  $1/Z_0$  ( $Z_0$  is the impedance of free space,  $(\mu_0/\epsilon_0)^{1/2}$ ) times the electric field for the electric-dipole, with the substitution  $\vec{p} \rightarrow \vec{m}/c$ . Similarly, the electric field for the magnetic-dipole source is the negative of  $Z_0$  times the magnetic field for an electric-dipole. Thus, we obtain the dipole fields

$$\vec{H} = \frac{1}{4\pi} \left\{ k^2 (\hat{n} \times \vec{m}) \times \hat{n} \frac{e^{ikr}}{r} + [3\hat{n}(\hat{n} \cdot \vec{m}) - \vec{m}] \left( \frac{1}{r^3} - \frac{ik}{r^2} \right) e^{ikr} \right\} \quad [4.7]$$

$$\vec{E} = -\frac{Z_0}{4\pi} k^2 (\hat{n} \times \vec{m}) \frac{e^{ikr}}{r} \left( 1 - \frac{1}{ikr} \right). \quad [4.8]$$

In the near-zone, the magnetic-dipole induced fields are approximated as

$$\vec{H} = \frac{1}{4\pi} \frac{3\hat{n}(\hat{n} \cdot \vec{m}) - \vec{m}}{r^3} \quad [4.9]$$

$$\vec{E} = \frac{iZ_0}{4\pi} k (\hat{n} \times \vec{m}) \frac{1}{r^2}. \quad [4.10]$$

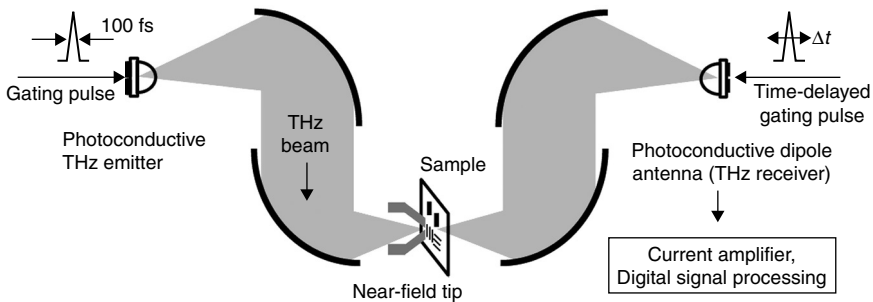
Needless to say, the magnetic field of the induced magnetic-dipole moment can be stronger than the incident magnetic field in case of the PEC case: the

electric field by the induced magnetic-dipole moment tends to be smaller than the incident electric field. It is noted that the fields in the near-zone are not only stronger, but contain more complex vector components than the far-fields, as shown in Figs 4.1 and 4.2. These fields are important in sensing subwavelength objects, such as single molecules, thin films, and biological features such as membranes.<sup>1-5</sup>

### 4.2 Terahertz near-field measurements

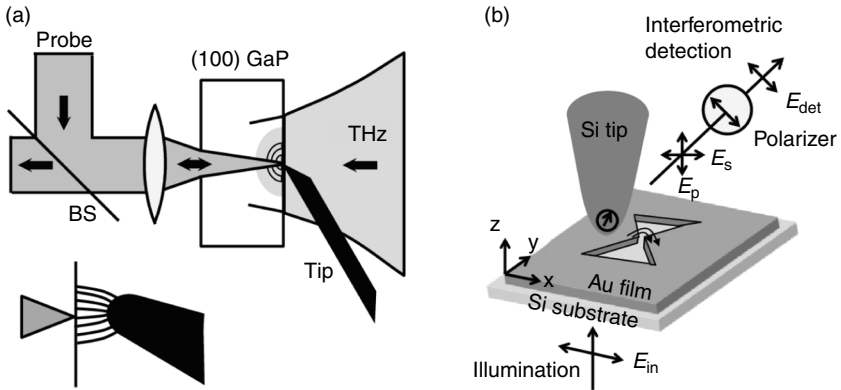
Near-field imaging with a subwavelength spatial resolution is obtained using different techniques in a wide spectral range from the visible to the THz frequency regime.<sup>6</sup> One way to improve the spatial resolution is to use an aperture made from a hole in a metal.<sup>7-14</sup> In 1998, the first demonstration of THz imaging with a spatial resolution about  $\lambda/4$  was reported by Hunsche *et al.*<sup>15</sup> As shown in Fig. 4.3, they focused the radiation into a tapered metal tip with a small aperture ( $d < 100 \mu\text{m}$ ) and scanned a sample in the near-field of this aperture.

Apertureless scanning near-field optical microscopy (ASNOM) is another near-field measurement technique, based on the idea that a subwavelength-sized metal tip can scatter light.<sup>16-18</sup> van der Valk *et al.* achieved a spatial resolution of  $18 \mu\text{m}$ , which corresponds to about  $\lambda/110$  for a wavelength of 2 mm. The THz pulses are focused onto a copper tip, which has been sharpened in a FeCl etch bath. The sharp copper tip locally distorts and concentrates the THz electric field (Fig. 4.4a).<sup>19</sup> Apertureless near-field imaging was originally developed at visible and mid-infrared wavelengths Schnell *et al.* also obtained the local near-field vector by scattering-type scanning near-field optical microscopy (SNOM) with a spatial resolution of about 10 nm in the mid-infrared regime (Fig. 4.4b).<sup>20,21</sup>



4.3 Experimental set-up for THz near-field scanning optical microscopes using a subwavelength aperture (adapted from Reference 15).

Copyrighted Material downloaded from Woodhead Publishing Online  
 Delivered by http://www.woodheadpublishingonline.com  
 Young-Mi Bahk (153-83-420)  
 Sunday, November 24, 2013 10:08:06 PM  
 IP Address: 147.46.44.138

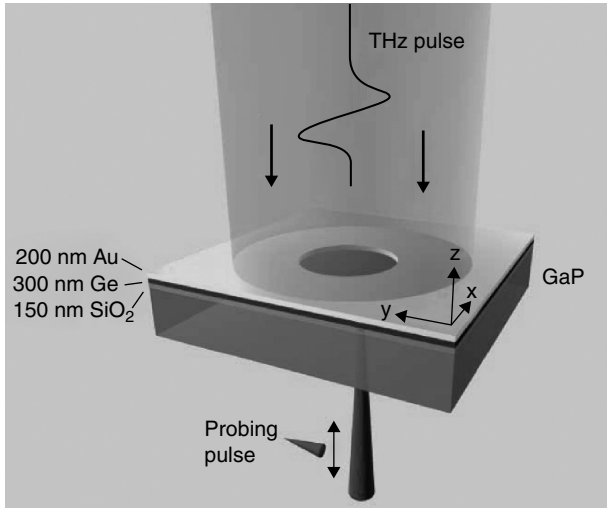


4.4 (a) Schematic of ASNM technique for THz imaging (adapted from Reference 19). (b) Scattering-type SNOM for a vectorial near-field mapping in mid-infrared frequency range (adapted from Reference 20). BS, beam splitter.

In both the aperture and the apertureless cases, the spatial resolution is determined by the aperture size or the tip radius curvature. For the aperture of radius  $a$ , the signal goes down as  $a^6/\lambda^4$ , which limits its effectiveness.<sup>22</sup> For the scattering off a sharp tip, to isolate scattering from the near-field only, high frequency tapping and heterodyne detection is needed.<sup>20,21</sup> In addition, there is the inevitable disturbance of the large tip affecting the environment. A more direct approach is to use an optical beam focused onto the near-field, to take advantage of (1) the naturally small spot size of the optical beam relative to the THz wavelength, and (2) the large wavelength separation between the optical regime and the THz regime, which limits interference and artifacts. For the optical beam to 'see' the THz field, the sample needs to be grown onto an electro-optic (EO) crystal such as GaP or ZnTe.

P. C. M. Planken's group reported on the measurement of the THz electric near-field behind a subwavelength-sized hole, which was directly integrated onto an EO detection crystal.<sup>23–25</sup> Figure 4.5 schematically shows the EO near-field imaging set-up when the sample is grown on GaP crystal. A quasi-near-field imaging can be achieved by the EO crystal being in mechanical contact with the sample, by pressing the sample gently on the crystal. This method has the advantage of being able to probe the evolution from the near-field to the far-field.

EO detection is based on a second-order nonlinear response of polarization in an EO material to an applied electric field.<sup>26,27</sup> A refractive index of the EO material is proportionally changed by the THz electric field. The birefringence causes a polarization change of the optical probe pulse that travels through the EO detection crystal. After the detection crystal, the probe beam passes through a quarter-wave plate which is oriented such that



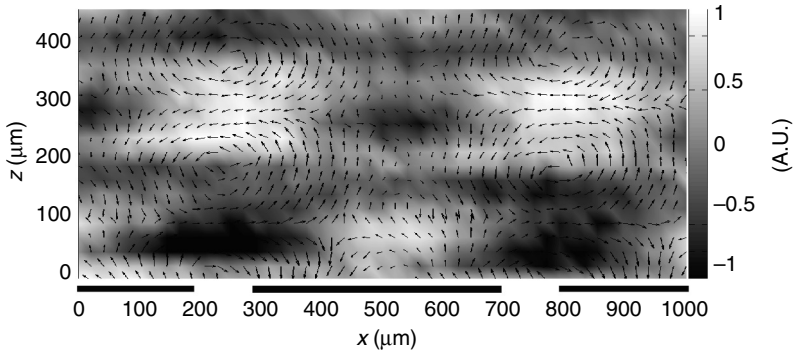
4.5 THz near-field microscopy set-up. EO sampling is used to measure the electric near-field of a subwavelength hole at each point. The local electric field is measured using the synchronized femtosecond optical probe beam. A germanium (Ge) and a SiO<sub>2</sub> layer prevent the probe beam from reflecting off the gold layer (adapted from Reference 28).

the originally linear polarization of the probe beam becomes circular. A signal proportional to the THz electric field is obtained by measuring the difference in the energy of two orthogonal polarization direction beams with a Wollaston prism and two photodiodes. For EO detection, zinblende crystals such as ZnTe and GaP are often used. By selecting the orientation of the detection crystal, it is possible to choose which component of the THz electric field vector the EO detection set-up is sensitive to. The *x*- and *y*-components of THz electric field are measured by a (110) or (111) crystal orientation, and the vertical component *E<sub>z</sub>* by a (001) oriented crystal. From the measurement of the three components of the electric field, measured as we move the sample away from the EO crystal, in this case GaP, one can calculate also the magnetic near-field, via the Maxwell’s equations,

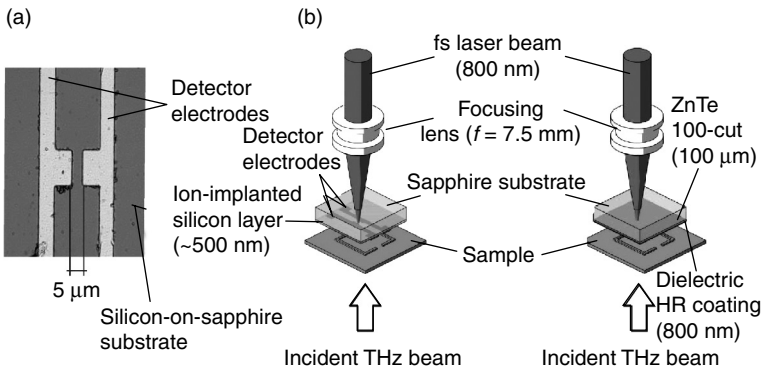
$$\nabla \times \vec{E} = -\frac{\partial \vec{B}}{\partial t}. \tag{4.11}$$

Figure 4.6 shows THz electric near-field vectors measured behind a metallic slit array with a width of 100 μm and a period of 500 μm when the incident beam comes from below.<sup>28</sup> The background grey color scale represents the *y*-component magnetic field, calculated from the measured electric field

Copyrighted Material downloaded from Woodhead Publishing Online  
 Delivered by http://www.woodheadpublishingonline.com  
 Young-Mi Bahk (153-83-420)  
 Sunday, November 24, 2013 10:08:06 PM  
 IP Address: 147.46.44.138



4.6 THz electric field and magnetic near-field profile at 1 THz for the slit array. The black line represents the electric field,  $E_x$  and  $E_z$ , and the background color denotes the magnetic field,  $B_v$ , calculated from the electric field. The measurements were performed as we moved the sample away from the crystal, defining  $z$  (adapted from Reference 28).



4.7 (a) Electrode structure of the detector antenna used as a THz near-field probe (from Reference 29). (b) Two different near-field detection techniques. Photoconductive antenna as polarization sensitive near-field probe (left) and nonlinear crystal as near-field probe (right) (adapted from Reference 30).

vectors by using Equation [4.11]. The black and white indicate negative and positive magnetic field amplitudes, respectively. This operational method has been adopted both in THz and in infrared (Andreas Bitzer and Markus B. Raschke).<sup>29–31</sup>

An alternative method is to use a small subwavelength-sized photoconductive antenna as a near-field probe, gated by a femtosecond optical pulse.<sup>29,30,32</sup> The detector antenna consists of an  $H$ -shaped electrode structure as shown in Fig. 4.7a deposited on a 500-nm-thick ion-implanted silicon-on-sapphire substrate. The system allows us to measure the in-plane electric and out-of-

Copyrighted Material downloaded from Woodhead Publishing Online  
 Delivered by http://www.woodheadpublishingonline.com  
 Young-Mi Bahk (153-83-420)  
 Sunday, November 24, 2013 10:08:06 PM  
 IP Address: 147.46.44.138

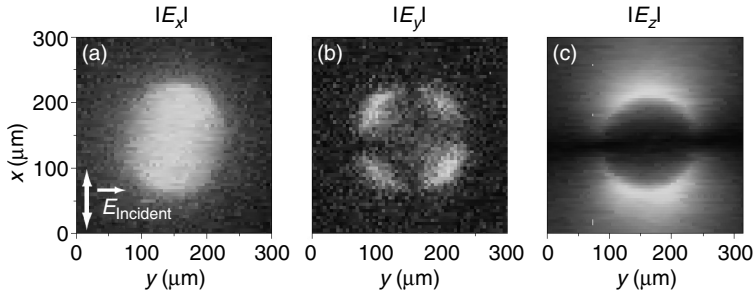
plane magnetic fields close to the sample with a spatial resolution on the micrometer scale ( $\sim\lambda/20$ ) at 0.5 THz (Fig. 4.7b, left). Out-of-plane electric field component can be measured using a detection scheme based on EO sampling in a nonlinear crystal (Fig. 4.7b, right). In the following chapters, we mainly focus on the EO sampling technique described in Fig. 4.5.

### 4.3 Near-fields of various subwavelength holes

Electromagnetic waves generally transmit through a single deep subwavelength hole with an efficiency below unity. This low transmission efficiency is due to poor coupling of subwavelength holes with radiative electromagnetic modes and the evanescent decay of the electromagnetic fields inside the holes.<sup>22,33</sup> However, the enhanced transmission in a single hole could be achieved by a bound cavity mode that couples resonantly to incident light or periodic corrugations of holes.<sup>34–37</sup> The transmission characteristics of light through various subwavelength holes and hole arrays in a metallic film have been the focus of much research activity around the world,<sup>37–42</sup> and it has been proved that the hole shape influences the optical transmission properties.<sup>43–49</sup> The near-field measurements can illustrate in detail how light interacts with the subwavelength hole and emerges from the hole. In this section, we will investigate the near-field characteristics for various subwavelength holes.

#### 4.3.1 Near-field imaging of circular holes

The electric fields, both in amplitude and in phase, passing through various holes are measured by the THz near-field time-domain spectroscopy (TDS) techniques. In 2009, Adam *et al.* reported on the measurement of all three electric field components,  $E_x(t)$ ,  $E_y(t)$  and  $E_z(t)$ , underneath subwavelength-sized circular holes.<sup>23,24</sup> These three components were measured by choosing a suitable probe-beam polarization and EO detection crystal orientation. They measured the  $x$ - and  $y$ -components by a (111) crystal orientation, and the  $z$ -component by a (100) crystal. The circular hole was fabricated in a 200-nm-thick gold layer deposited onto a GaP detection crystal with a thickness of 300  $\mu\text{m}$ . The results can be seen in Fig. 4.8 with amplitude images of the  $x$ -,  $y$ - and  $z$ -components of the measured THz electric near-field at 0.2 THz for a single circular hole, with a diameter of 150  $\mu\text{m}$ . The scan area is 315  $\mu\text{m}$  by 315  $\mu\text{m}$  and the spatial resolution is about 10  $\mu\text{m}$ . The figure shows that the  $x$ -component of electric field is strongest in the middle of the hole. The  $y$ -component of the field exhibits a quadrupole mode consisting of four lobes, in which adjacent lobes are out of phase. Finally, the  $z$ -component of the field is concentrated at the top and bottom edges of the hole, which are out of phase of each other.



4.8 THz electric near-field for a single circular hole with a diameter of 150 μm at 0.2THz. Figures (a)–(c):  $|E_x|$ ,  $|E_y|$  and  $|E_z|$  (adapted from Reference 24).

These results can be understood by the predictions made by Bouwkamp because metals act as perfect conductors in THz frequency regime.<sup>22,50</sup> The diffraction of electromagnetic radiation by a subwavelength hole was first treated by Bethe.<sup>22</sup> He studied the electromagnetic coupling through a very small hole in the idealized case of a zero-thickness perfect conductor film perforated with a circular hole of radius  $a$ . However, some important details of the field distribution in the near-zone cannot be explained by his model: subsequent higher-order corrections were calculated by Bouwkamp. From his calculations, we see that, inside the hole ( $\rho < a$ ) at normal incidence, the tangential components of  $E$  vary rapidly over the surface of the hole,

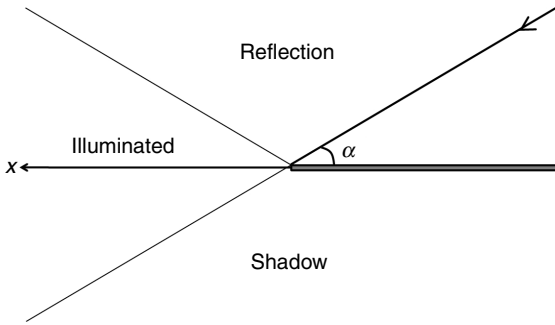
$$E_x = -\frac{4ik}{3\pi} \frac{2a^2 - \rho^2 (1 + \sin^2 \phi)}{(a^2 - \rho^2)^{1/2}} E_{inc}, E_y = -\frac{2ik}{3\pi} \frac{\rho^2 \sin 2\phi}{(a^2 - \rho^2)^{1/2}} E_{inc}, E_z = 0 \quad (\rho < a). \tag{4.12}$$

He also calculated the field on either face of the screen in the vicinity of the hole. In his model, the electric near-field of a hole at the shadow is written as

$$E_x = 0 \quad E_y = 0 \quad E_z = \frac{4ika^3}{3\pi} \frac{\cos \phi}{\rho(\rho^2 - a^2)^{1/2}} E_{inc} \quad (\rho > a). \tag{4.13}$$

Near the boundary  $\rho = a$ , the normal component of  $E$  has weak singularities. This is analogous to a weak, integrable singularity occurring frequently at two-dimensional sharp edges for example, in Sommerfeld’s solution of the diffraction by a half-plane. In 1896, Sommerfeld treated the two-dimensional case of a plane wave incident on an infinitely thin,

Copyrighted Material downloaded from Woodhead Publishing Online  
 Delivered by http://www.woodheadpublishingonline.com  
 Young-Mi Bahk (153-83-420)  
 Sunday, November 24, 2013 10:08:06 PM  
 IP Address: 147.46.44.138



4.9 Diffraction of a plane wave by a perfectly conducting half-plane (adapted from Reference 51).

perfectly conducting half-plane, as shown in Fig. 4.9. He theoretically discussed the diffraction by a narrow slit when the magnetic field vector is parallel to the edges of the slit. The following equation shows that the electromagnetic fields have singularities occurring at a sharp edge with a normal incident light ( $\alpha = 90^\circ$ ):

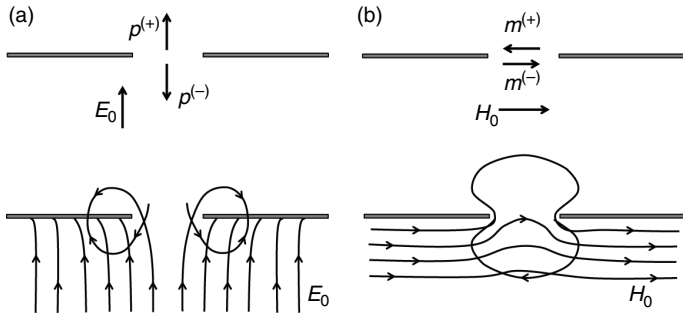
$$E_x(x, t) = \frac{E_0}{\sqrt{2\pi}} \sqrt{\frac{\lambda}{x}} e^{-i\omega t} e^{-i\frac{\pi}{4}}, \tag{4.14}$$

where  $\epsilon_0$  is the vacuum permittivity,  $E_0$  the incident electric field,  $\omega$  the angular frequency, and  $x$  the distance from the edge, respectively. The field singularity at  $x = 0$  for this half-plane is the origin of the weak singularities at the edge of the circular hole.

### 4.3.2 Effective dipole moments of circular holes

The near-fields described in the previous section are closely related to the surface currents and surface charges around the hole, which constitute the source of the far-field radiation. Closer examination reveals that these sources mimic pseudo-electric and magnetic-dipoles, as shall be shown. When the hole is small compared to wavelength, the problem of radiation from the hole can be described as a quasi-static boundary value problem. The boundary value problem is specified by the *normal* electric field  $E_{0,nor}$  and the *tangential* magnetic field  $H_{0,tan}$  that would exist in the absence of the aperture. This is not surprising, since the tangential magnetic field and the normal electric fields are what survive at the metal interface with their amplitudes *twice* the incident fields by reflection. When solving the mixed boundary condition problems, the near-fields are represented by a multi-pole expansion.<sup>52</sup> The field lines shown in Fig. 4.10a and b are the sum of the

Copyrighted Material downloaded from Woodhead Publishing Online  
 Delivered by http://www.woodheadpublishingonline.com  
 Young-Mi Bahk (153-83-420)  
 Sunday, November 24, 2013 10:08:06 PM  
 IP Address: 147.46.44.138



4.10 The effective (a) electric- and (b) magnetic-dipole moments, as viewed from above and below the surface (top). The field lines can be described by fictitious dipoles added to the initial fields without the hole (bottom) (adapted from Reference 52).

straight field lines in the absence of the hole, and the fictitious dipoles of the magnitudes

$$\vec{p}_{\text{eff}} = \pm \frac{4\epsilon_0 a^3}{3} \vec{E}_{0,\text{nor}}, \vec{m}_{\text{eff}} = \mp \frac{8a^3}{3} \vec{H}_{0,\text{tan}}, \tag{4.15}$$

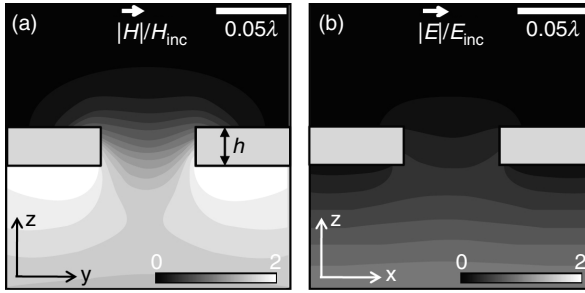
where the plus and minus signs are chosen according to whether we are describing the field lines above the hole or below. Figure 4.10 shows how the electric and magnetic field lines distort to give rise to the dipole field.

The concept of effective dipole moments to describe the electromagnetic properties of small holes was developed by Bethe.<sup>22</sup> From his calculation of the first-order diffracted field, the diffraction cross-section is proportional to

$$\begin{aligned} \pi a^2 \left( \frac{64}{27\pi^2} k^4 a^4 \right) \left( 1 + \frac{1}{4} \sin^2 \theta \right) &= \pi a^2 \left( \frac{1024}{27} \pi^2 \frac{a^4}{\lambda^4} \right) \left( 1 + \frac{1}{4} \sin^2 \theta \right) \\ &\approx \pi a^2 \left[ 374 \left( \frac{a}{\lambda} \right)^4 \right] \left( 1 + \frac{1}{4} \sin^2 \theta \right) \end{aligned}$$

where  $a$  is the radius,  $\lambda$  the wavelength,  $k = 2\pi/\lambda$ ,  $\theta$  the incidence angle, and TM (transverse magnetic) polarization is assumed. Note the large factor of 374 in front of the well known  $(a/\lambda)^4$  term, which softens somewhat the rapid decrease of the cross-section with decreasing size for subwavelength holes.

Copyrighted Material downloaded from Woodhead Publishing Online  
 Delivered by http://www.woodheadpublishingonline.com  
 Young-Mi Bahk (153-83-420)  
 Sunday, November 24, 2013 10:08:06 PM  
 IP Address: 147.46.44.138



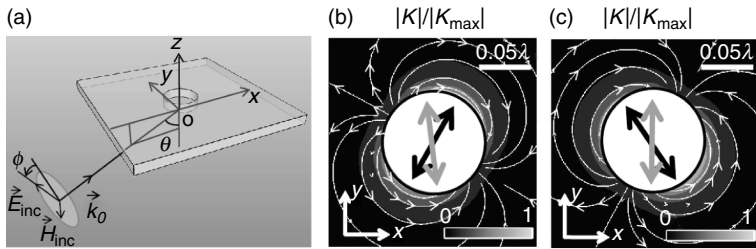
4.11 Normalized (a) tangential magnetic and (b) tangential electric field distributions for the normal incidence, for a finite-thickness PEC film calculated by the finite-difference-time-domain (FDTD) technique. The results are essentially the same for normal incidence and oblique incidences (adapted from Reference 53).

Experimentally, it is meaningful to devise a means to test whether the Bethe’s concept holds for realistic subwavelength holes. To this end, we briefly examine subwavelength holes at optical frequency. Recently, Kihm *et al.* studied near- and far-field radiation of a subwavelength circular hole on a *finite-thickness* PEC plane.<sup>53</sup> While the singularities are largely softened by the finite thickness some salient features remain. The tangential magnetic field enters the subwavelength hole with a certain distortion (Fig. 4.11a), with its amplitude at the center of the aperture equal to that of the incident field. In contrast, the tangential electric field is primarily reflected, its influence being much weaker on both sides of the plane and inside the hole (Fig. 4.11b). Therefore, the scattering properties of an aperture in a metal film are mainly determined by the incident magnetic field-induced surface currents, which in turn function as a source for the far-field radiation.

The best way to separate the effects of the incident electric and magnetic fields on the metallic hole is to probe the structure with light at oblique-incidence angles, having an asymmetric polarization that is neither purely transverse electric (TE,  $\phi = 0^\circ$ ) nor transverse magnetic (TM,  $\phi = 90^\circ$ ), where  $\phi$  is the polarization angle (Fig. 4.12a). In this case, the incident electric and magnetic fields projected onto the reflecting plane,  $\vec{E}_t = \vec{E}_{inc} - (\hat{z} \cdot \vec{E}_{inc})\hat{z} = E_{inc}(-\cos\theta\sin\phi, \cos\phi, 0)$  and  $\vec{H}_t = H_{inc}(-\cos\theta\cos\phi, -\sin\phi, 0)$  are, in general, not orthogonal, which creates an ideal situation to discriminate the electric and magnetic nature of the scattering.

Figure 4.12b and c show finite-difference-time-domain (FDTD) calculations of surface currents on the scattering side of the structure, for the case of an oblique incident angle ( $\theta = 80^\circ$ ) with two polarization states,

Copyrighted Material downloaded from Woodhead Publishing Online  
 Delivered by http://www.woodheadpublishingonline.com  
 Young-Mi Bahk (153-83-420)  
 Sunday, November 24, 2013 10:08:06 PM  
 IP Address: 147.46.44.138



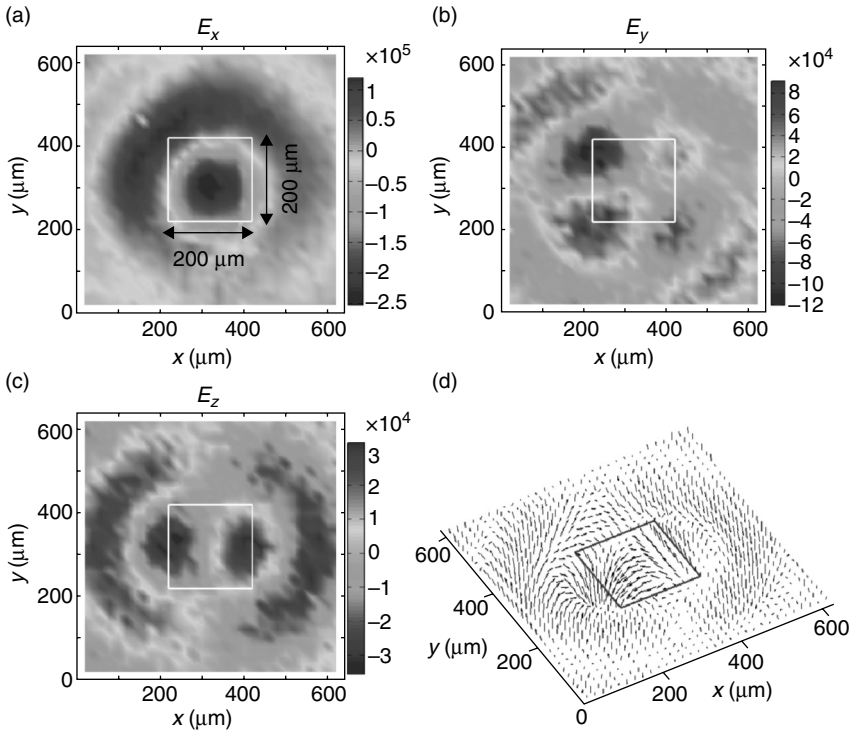
4.12 (a) Schematic of set-up with an oblique incidence. (b, c) Surface current distribution on the exit side of the hole for  $\phi = 21^\circ$  and  $159^\circ$  with fixed  $\theta = 80^\circ$ , respectively.  $\vec{E}_i$  and  $\vec{H}_i$  are depicted as gray and black arrows inside the hole, respectively. The white arrows represent the direction of the surface current (adapted from Reference 53).

$\phi = 21^\circ$  and  $159^\circ$ , respectively.  $\vec{E}_i$  and  $\vec{H}_i$  are depicted by gray and black arrows, respectively. For both cases, the surface current  $\vec{K}$  profile is aligned perpendicularly to the tangential magnetic field, with the incident electric field direction being essentially irrelevant. Continuous changing of the electric field direction while maintaining the magnetic field direction can be achieved by varying the wave vector of the incident light with almost no effect on the surface current distribution. These observations strongly suggest that the surface currents on the scattering side of the structure are of an induced nature, with symmetric axis determined by the incident magnetic field direction  $\hat{n} \times \vec{H}_i$ , where  $\hat{n}$  is the unit vector normal to the plane, in this case  $\hat{z}$ .

With the surface current profile on the scattering side determined primarily by the incident magnetic field, the far-field radiation polarization also reflects the magnetic field orientation. As its far-field polarization is largely invariant with respect to changes in the incident electric field, the subwavelength aperture, when combined with far-field polarization analysis, senses the orientation of the magnetic vector field. The incident magnetic field direction can be obtained simply by rotating the polarization of the scattered light by  $90^\circ$ . It is expected that oblique-incidence, non-TM/TE polarization THz imaging will reveal the same trends.

### 4.3.3 Near-field imaging of square holes

Hole shapes are obviously important in terms of near-field enhancements. In terms of symmetry, the square hole most closely resembles a circular hole, and Fig. 4.13a, b, and c represent  $x$ -,  $y$ -, and  $z$ -components of electric field distribution for a single square hole at 1.44 THz, when the incident field

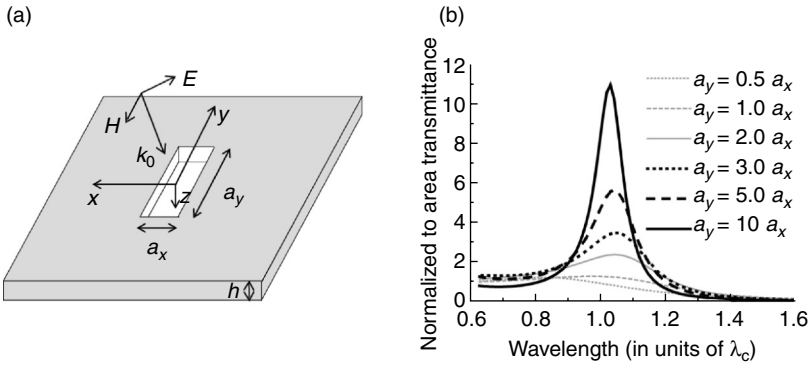


4.13 (a)  $x$ - (b)  $y$ - and (c)  $z$ -components of electric field distribution for single square hole at 1.44THz are represented. (d) Three-dimensional vector mapping of the electric field distribution. The size of square hole is about 200  $\mu\text{m}$  punctured on 80- $\mu\text{m}$ -thick Al plate, and an EO sampling was performed with the crystal in close contact.

polarization is along the  $x$ -direction. The size of the square hole is about 200  $\mu\text{m}$  deposited on 80- $\mu\text{m}$ -thick Al plate. In Fig. 4.13d, the black arrows denote a three dimensional vector mapping of the electric field for the single square hole. The figure demonstrates that the  $E_x$  component is mostly localized inside the square hole, whereas the  $y$ - and  $z$ -components of the field are mostly confined to the edges of the hole, closely resembling the images for the circular hole.

#### 4.3.4 Near-field imaging of rectangular holes

Both the square hole and circular hole are poor antennas and their singularities are of an integrable kind, which limits the field enhancements. One way to dramatically increase the field enhancement is to make the aperture a strongly asymmetric rectangle, which supports a well-defined transmission



4.14 (a) Schematic of a single rectangular hole of sides  $a_x$  and  $a_y$  perforated on a metal film of thickness  $h$ . (b) Normalized-to-area transmittance versus wavelength (in units of the cut-off wavelength  $\lambda_c = 2a_y$ ), for a normal incident plane wave impinging on a rectangular hole, for different ratios  $a_y/a_x$  (adapted from Reference 34).

resonance for light polarized along its short side. F. J. Garcia-Vidal *et al.* have shown numerically that a single rectangular hole exhibits strong transmission resonances near their cut-off wavelengths<sup>34</sup>. Figure 4.14a shows schematically the system: a rectangular hole of sides  $a_x$  and  $a_y$  perforated on a metallic film of thickness  $h$ . The structure is illuminated by  $p$ -polarized light and the metal is treated as a PEC, a good approximation in the THz frequency regime. Figure 4.14b depicts the calculated normalized-to-area transmission spectra for rectangles in which the aspect ratio ( $a_y/a_x$ ) is varied between 1 (square hole) and 10. The thickness of the metallic film is fixed in all cases at  $h = a_y/3$ . As the ratio  $a_y/a_x$  is increased, a transmission peak develops close to the cut-off wavelength ( $\lambda_c = 2a_y$ ), with increasing maximum transmittance and decreasing linewidth. The physical origin of the transmission resonances appearing at  $\lambda_{res} = \lambda_c$  stems from the excitation of a Fabry–Pérot resonance in which the propagation constant is zero. An analytical approximation for the transmittance at resonance  $T_{res}$  can be obtained by

$$T_{res} \approx \frac{3}{4\pi} \frac{\lambda_{res}^2}{a_x a_y} \approx \frac{3}{\pi} \frac{a_y}{a_x}. \tag{4.16}$$

It is noted that the transmission cross-section of a rectangular hole is given by the square of the long ( $a_y$ ) sides of the rectangle at the resonance, so that it is proportional to  $\lambda_{res}^2$ ,  $\sigma_{res} \approx 3/4\pi \lambda_{res}^2$ . A close analogy is found in bound charges with losses only through radiation (radiation damping),

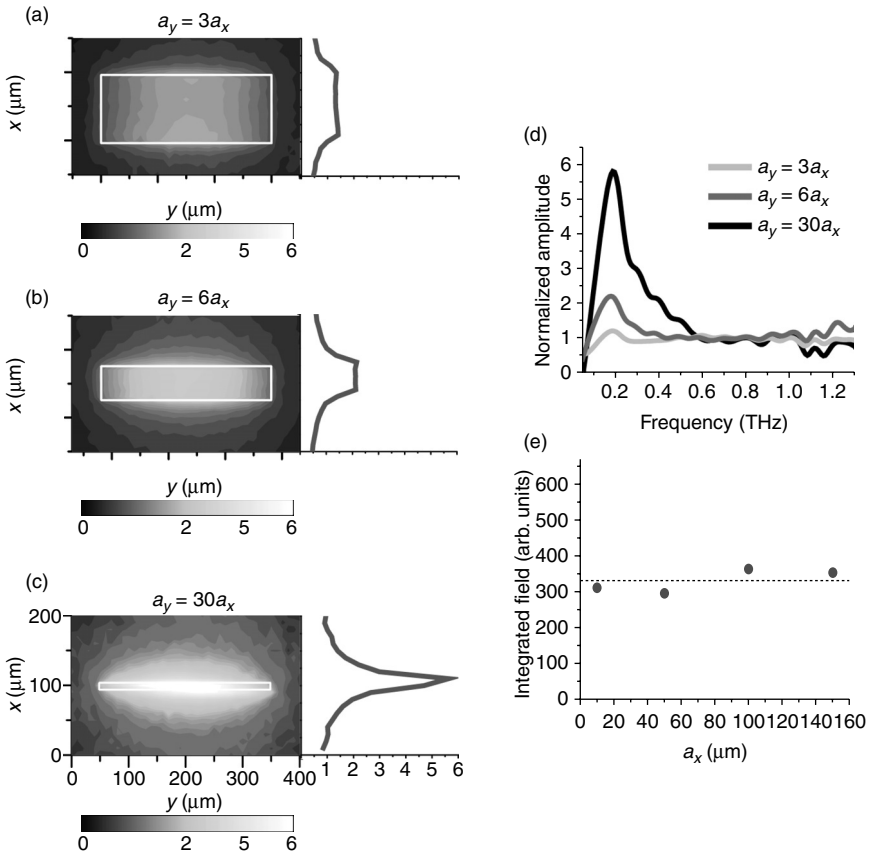
whose resonant cross-section is also proportional to  $\lambda_{\text{res}}^2$ ,  $\sigma_{\text{res}} \approx (3/2\pi)\lambda_{\text{res}}^2$ . The cross-section of the rectangle is half this value because we are only looking at the transmittance, not reflection. The electric field enhancement has also the form resembling Equation [4.16], because both energy and amplitude enhancements are essentially the same, the magnetic field amplitude being almost identical to the incident one. The electric field enhancement can be verified by near-field imaging experiments.

In 2007, Seo *et al.* experimentally verified the occurrence of a large field enhancement through the rectangular hole in the THz frequency range, using THz Fourier-transform near-field imaging with  $\sim\lambda/100$  resolution.<sup>54</sup> They could measure the component parallel to the short side of rectangle, that is, the main near-field component. Figure 4.15a, b and c are images for samples with  $a_x = 100, 50$  and  $10 \mu\text{m}$  respectively for a fixed length of  $a_y = 300 \mu\text{m}$  at 0.2 THz, which is the approximated resonant frequency. These figures show that the near-field amplitude becomes proportionally stronger as the rectangular hole becomes narrower. The field enhancement increases with the increasing aspect ratio of the rectangular hole,  $a_y/a_x$ , and therefore with decreasing width of the rectangle (Fig. 4.15d). Figure 4.15e shows that the area-integrated field amplitude remains nearly constant for different rectangle widths. It strongly suggests that the same amount of the energy passes through a narrow rectangular hole, confirming the funneling of energy in the near-field.

#### 4.3.5 Near-field imaging of rectangular holes with nano-sized width

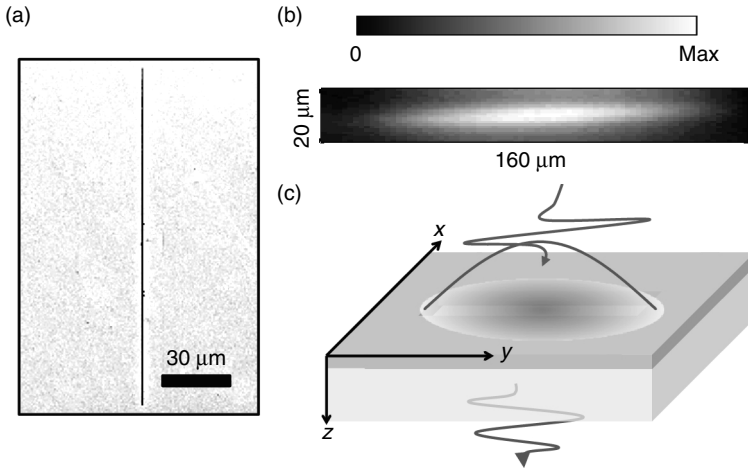
In the previous section, the rectangular hole structures had micron-sized widths. In this regime, it has been shown, theoretically and experimentally, that the field enhancement inside holes increases as the width decreases. A natural question is whether this field enhancement will keep going up as we decrease the width to nanoscale.

In this section, we will image long rectangular holes with nano-sized widths, called THz nanoantennas or THz nanoresonators, with a spatial resolution of  $10 \mu\text{m}$ . The samples were fabricated by Dai-Sik Kim's group and THz near-field imaging experiments were performed by A. J. L. Adam at TU-Delft. This structure was shown to induce field enhancement in the range of a few hundred for the fundamental resonance,<sup>55</sup> estimated by the Kirchhoff integral formalism (Section 4.4). These THz nanoantennas with a striking aspect ratio funnel THz electromagnetic waves through, accompanied by a large field enhancement unavailable for micron-sized width. THz nanoantennas with giant field enhancement open a strong possibility of potential applications, such as broadband field enhancement and nonlinear devices, filters, detectors and active switching device.<sup>56-60</sup>



4.15 x-component of electric near-fields around single rectangles of different widths for fixed length, patterned on top of the EO crystal (GaP). The plotted images are shown for (a)  $a_x = 100 \mu\text{m}$ , (b)  $a_x = 50 \mu\text{m}$  and (c)  $a_x = 10 \mu\text{m}$ . The length is fixed at  $300 \mu\text{m}$ . The black line on the right side is cut through the center of the rectangular hole. (d) The spectra at the center of the rectangle for various aspect ratios are shown. (e) The integrated field amplitude over the area of the rectangle versus the width of the rectangle is shown (adapted from Reference 54).

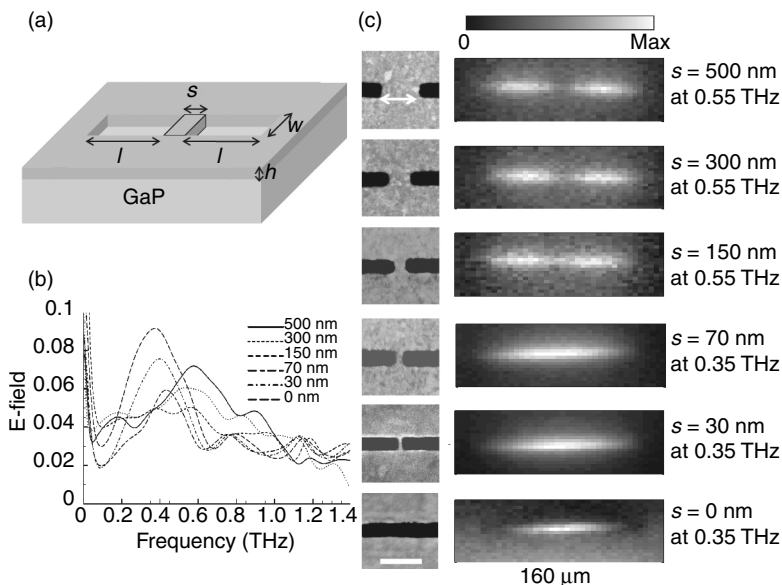
Figure 4.16a shows a scanning electronic microscope (SEM) image of a THz nanoantenna with a length of  $150 \mu\text{m}$  and a width of  $120 \text{ nm}$ . The samples are grown on a  $300\text{-}\mu\text{m}$ -thick (110) oriented GaP EO detection crystal to measure the  $x$ -component of the electric near-field. Figure 4.16b shows the electric near-field imaging at resonance frequency, showing a fundamental mode at the frequency of  $0.35 \text{ THz}$ . These modes are schematically described in Fig. 4.16c.



4.16 (a) SEM image of THz nanoantenna with a length of 150  $\mu\text{m}$  and a width of 120 nm. (b) x-component of electric near-field at resonance frequency of 0.35 THz. (c) Schematic of the fundamental mode.

Using this THz near-field method, we can also see a coupling between two THz nanoantennas separated by sub-skin depth barriers. Shown in Fig. 4.17a, two THz nanoantennas are vertically aligned with a metallic nanoscale barrier. Normally, the coupling between two vertically aligned nanoantennas has been ignored, because the coupling between parallelized dipoles is relatively weak compared to that between serialized dipoles. Hyeong-Ryeol Park *et al.*, however, have shown that the coupling between the paired nanoantennas changes drastically, as the width of the metallic barrier decreases below the skin depth, about 100 nm in the THz regime.<sup>61</sup> The resonance is expected to change from  $\omega$  to  $\omega/2$  as the nanobarrier widths fall below the skin depth ( $\omega$  corresponds to the fundamental mode of each resonator with length  $l$ , but influenced also by the index of refraction of GaP). This is because the strongly enhanced resonant electric field inside each nanoantenna can penetrate through the sub-skin depth barrier, coupling the adjacent modes, and generating a new resonant mode. Shown in Fig. 4.17b are the near-field spectra of two equal-length THz nanoantennas with a length of 75  $\mu\text{m}$  and width of 120 nm, taken at the center point. Nanobarriers with widths of  $s = 0, 30, 70, 150, 300$  and 500 nm separate the two nanoantennas. We start to see significant red-shift in the resonant transmission peak at the barrier width 150 nm, close to the skin depth of gold. For the thinnest 30 nm wide nanobarrier, it is noted that indeed, the resonance frequency converges to  $\omega/2$ . It can also be confirmed by THz near-field imaging, as shown in Fig. 4.17c.

Copyrighted Material downloaded from Woodhead Publishing Online  
 Delivered by http://www.woodheadpublishingonline.com  
 Young-Mi Bahk (153-83-420)  
 Sunday, November 24, 2013 10:08:06 PM  
 IP Address: 147.46.44.138



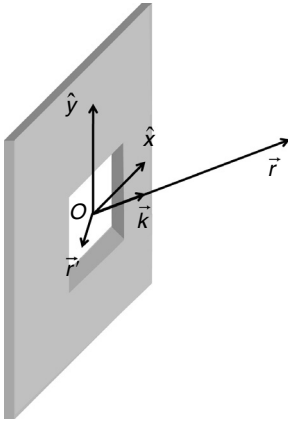
4.17 (a) Schematic of a metallic nanobarrier with width  $s$  between the two THz nanoantennas with a length  $l$  and a width  $w$  fabricated on a thin gold film with a thickness of  $h$ . GaP crystal is used as substrate for THz near-field measurement. (b) Spectra of electric fields measured at the metallic barrier region of the coupled THz nanoantennas ( $l = 75 \mu\text{m}$  and  $w = 120 \text{ nm}$ ). The barrier widths( $s$ ) are 0, 30, 70, 150, 300 and 500 nm. (c) SEM images (left) and x-component of electric near-fields (right) for six cases of the paired THz nanoantennas considered in (b). The scale bar is 500 nm.

## 4.4 Kirchhoff formalism for near-field estimate

Far-field transmissions exceeding the areal coverage, caused by strong near-field enhancements of subwavelength holes have been reported in a wide spectral range from the visible to the THz frequency regime. The estimation of near-field enhancement via the far-field transmission is achieved without direct near-field measurements.<sup>62</sup>

### 4.4.1 Kirchhoff formalism and the relation between near- and far-fields

The relation between the near- and the far-field is derived from the Kirchhoff integral formalism. When an observation point is located far



4.18 Diffraction geometry for a screen with a square aperture (adapted from Reference 62).

from the hole, the diffracted electric field can be approximated by the Kirchhoff integral,

$$\vec{E}(\vec{r}) = \frac{ie^{i\vec{k}\cdot\vec{r}}}{2\pi r} \vec{k} \times \int_A \hat{n} \times \vec{E}(\vec{r}') e^{-i\vec{k}\cdot\vec{r}} da', \tag{4.17}$$

where  $\vec{r}'$  is the coordinate of the element of the surface area of the hole,  $A$ ;  $\vec{r}$  is the distance from origin,  $O$ , to the observation point;  $\hat{n}$  is the surface normal and  $\vec{k}$  is the wave vector in the direction of the observation point, as indicated in Fig. 4.18.

For an incident beam polarized in the horizontal direction and impinging upon the hole at the normal incidence, we can use the scalar expression and define the diffracted horizontal component of electric fields,

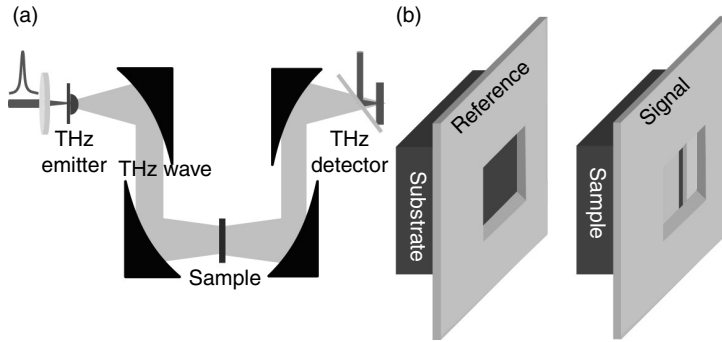
$$E_{\text{far}} = \frac{e^{ikr}}{i\lambda r} \int_A E_{\text{near}}(r') da' = \frac{e^{ikr}}{i\lambda r} \langle E_{\text{near}} \rangle A, \tag{4.18}$$

where the bracket means the averaged near-field over the aperture area, that is,

$$\langle E_{\text{near}} \rangle = \frac{1}{A} \int_A E_{\text{near}}(r') da'. \tag{4.19}$$

According to this formalism, the transmitted far-field through the hole is proportional to the near-field distribution inside the hole.

Copyrighted Material downloaded from Woodhead Publishing Online  
 Delivered by http://www.woodheadpublishingonline.com  
 Young-Mi Bahk (153-83-420)  
 Sunday, November 24, 2013 10:08:06 PM  
 IP Address: 147.46.44.138



4.19 (a) Typical THz far-field set-up. (b) Schematics of a reference aperture with substrate (typically Si, quartz, sapphire or SiN membrane) only (left), and with a metallic sample grown on the same substrate (right).

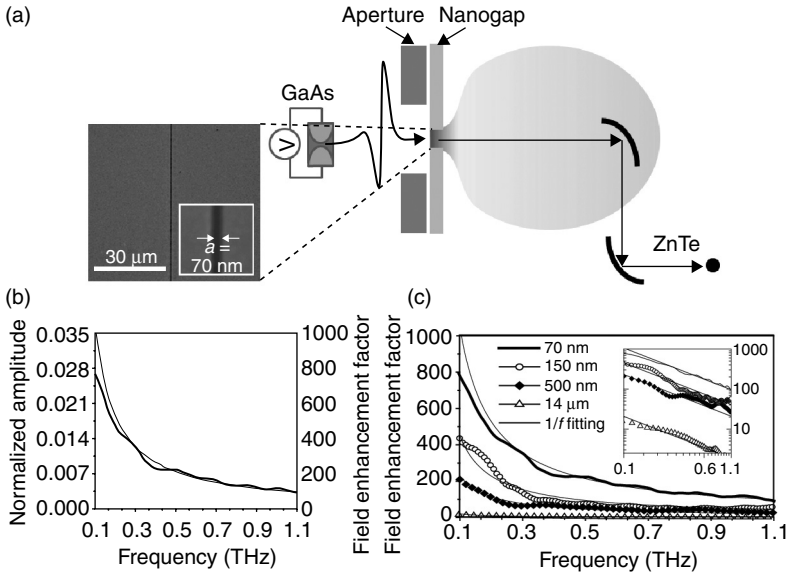
Figure 4.19a shows the typical set-up for the measurement of the transmitted far-field THz wave.<sup>55,63</sup> The transmission through the sample is experimentally characterized by the normalized amplitude,  $\alpha(\omega)$ , defined as the ratio between the transmitted amplitude through the substrate only on the reference aperture, and that through the sample (Fig. 4.19b).

$$\alpha(\omega) = \frac{|E_{\text{far}}^{\text{signal}}(\omega)|}{|E_{\text{far}}^{\text{reference}}(\omega)|} = \frac{|\langle E_{\text{near}}^{\text{reference}}(\omega) \rangle \cdot w \cdot l|}{|\langle E_{\text{near}}^{\text{reference}}(\omega) \rangle \cdot A|} = \frac{|\langle E_{\text{near}}^{\text{signal}}(\omega) \rangle|}{|\langle E_{\text{inc}}(\omega) \rangle|} \cdot \beta \quad [4.20]$$

It follows therefore that the near-field enhancement can be estimated from the far-field measurement, corresponding to  $\alpha(\omega)/\beta$ , where  $\beta$  is the hole-to-aperture area ratio.

#### 4.4.2 Near-field estimate of nanoslit and nanoantenna

In 2009, a  $10^3$  field enhancement inside a very narrow slit was demonstrated by measuring the transmitted far-field in the THz regime.<sup>63</sup> Figure 4.20a presents a schematic of the experiment set-up. The sample consisted of a nanoslit (width  $w = 70$  nm) fabricated using a focused ion beam on the 60-nm-thick gold film. To obtain a normalized transmitted amplitude through the nanoslit, they performed THz far-field TDS with single-cycle THz source generated from a 2 kV/cm biased semi-insulating GaAs emitter. The emitter was illuminated by a femtosecond Ti:sapphire laser pulse train with center-wavelength 780 nm, a 76 MHz repetition rate and a 130 fs pulse width. An EO sampling method was used to detect the transmitted THz waves in the time domain, in which an optical probe pulse underwent



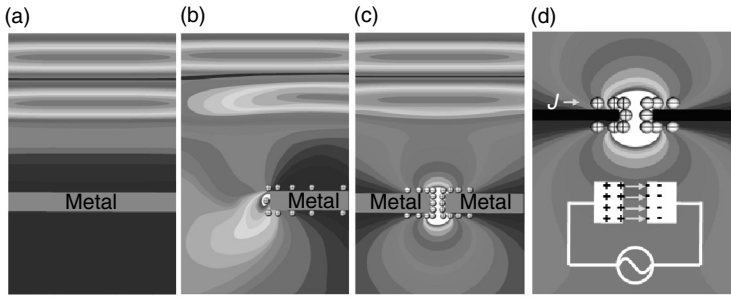
4.20 (a) SEM image of a 70-nm-width nanogap perforated on gold film and THz-TDS using EO sampling for detection of far-field transmitted amplitudes. (b) Normalized amplitude and field enhancement shown on the right-hand axis. (c) Field enhancement through samples with various gap widths:  $a = 70, 150, 500$  nm and  $14 \mu\text{m}$ , where  $h = 60, 150, 60$  nm and  $17 \mu\text{m}$ , respectively (inset: a log-log plot) (adapted from Reference 63).

a slight polarization rotation by the synchronized THz beam in a (110) oriented ZnTe crystal, detecting the horizontal electric field.

The transmitted far-field amplitude is connected to the enhanced near-field amplitude at the gap through Kirchhoff integral formalism, described in the previous section. Figure 4.20b shows  $\alpha(\omega)$  for the nanogap sample, reaching 2.7% at the lowest frequency of 0.1 THz. The nanogap-to-aperture area ratio,  $\beta = \text{width}(\text{nanogap})/\text{width}(\text{aperture})$ , is only 0.0035% = 70 nm/2 mm. From these results, they could obtain the near-field enhancement inside the gap, a factor of 800. They also proved that the electric field increases with decreasing slit width (Fig. 4.20c). This field enhancement is caused by two Sommerfeld half-planes closely approaching, creating a steeper singularity.

When an electromagnetic wave impinges on a perfect electrically conducting plane at normal incidence, current is induced on the surface, with no charge accumulating anywhere. When this plane is cut into Sommerfeld half-planes, charges accumulate at the edges within a scale length of one wavelength, so that the surface charge density has a singularity at  $x = 0$ . When the two metallic half-planes are brought back together, charges at both sides

Copyrighted Material downloaded from Woodhead Publishing Online  
 Delivered by http://www.woodheadpublishingonline.com  
 Young-Mi Bahk (153-83-420)  
 Sunday, November 24, 2013 10:08:06 PM  
 IP Address: 147.46.44.138

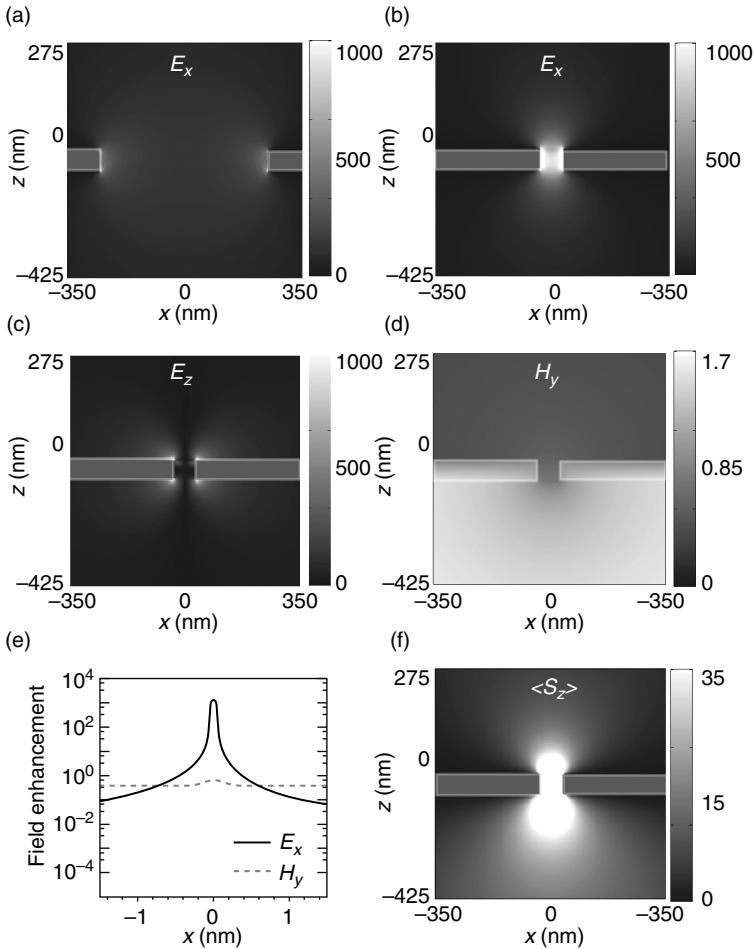


4.21 THz nanogap concept. (a) A conducting plane excited by normal incidence light. (b) A half-plane. (c) A nanogap. (d) A capacitor-like charging of the nanogap.

attract each other with increasing strength as the slit width decreases. This implies a capacitor-like charging of the nanogap (Fig. 4.21).

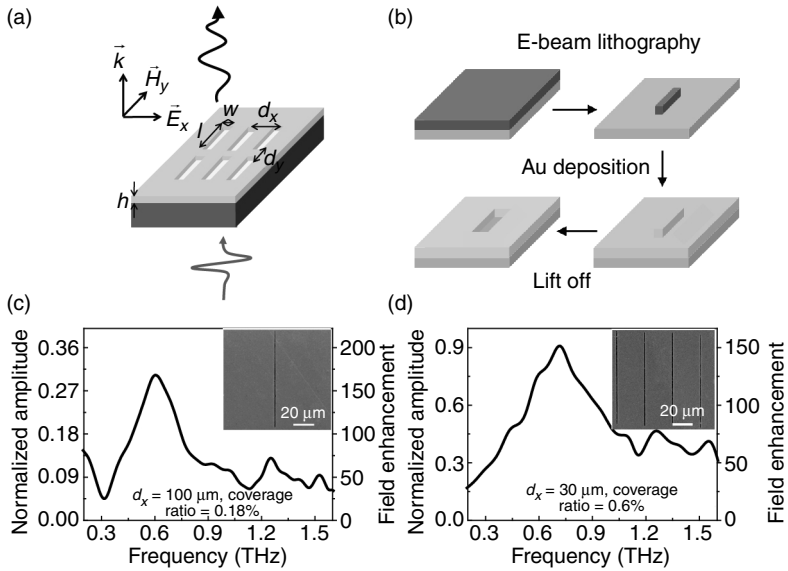
To understand these phenomena occurring near the nanoslit, a two-dimensional FDTD analysis was carried out. Figure 4.22a and b show an increasing field enhancement with a decreasing gap beyond the skin depth regime. It is in close agreement with the experimental results. While the horizontal electric field at the gap is orders of magnitudes stronger, the magnetic field stays mostly on the order of 1, but with a very small radius of curvature resulting in an enormous curl. To see the energy flow through the nanoslit, Fig. 4.22f plots the time-averaged Poynting vector  $\langle S_z \rangle$  where concentration of light energy at the sub-skin depth gap is apparent. What is striking is that the Poynting vector enhancement is much smaller than what simple multiplication of electric and magnetic fields suggests, indicating that the phase difference between the enhanced electric field and impinging magnetic fields is close to  $90^\circ$  in this quasi-static regime.

Field enhancements in rectangular holes can also be better estimated by Kirchoff formalism than by direct imaging described in Section 4.3, where the high frequency plateau was assumed to have the same amplitude as the incident field. Park *et al.* present a giant field enhancement of the THz electric component through THz nanoantennas which are hundreds of microns in length and have nano-sized widths,<sup>55</sup> using Kirchoff formalism. They considered an array of rectangular holes with  $w = 200$  nm and  $l = 100$   $\mu\text{m}$  in a metallic film with thickness  $h = 100$  nm on a dielectric substrate of 450- $\mu\text{m}$ -thick undoped silicon, as shown in Fig. 4.23a. These THz nanoantennas, acting as resonators in THz frequency range, have the maximum field enhancement of about 150 at the resonance frequency of 0.6 THz, which is  $\sim c/(2n_{\text{eff}}l)$ , where  $n_{\text{eff}}$  is the effective refractive index of the air-substrate composite.<sup>63</sup> The samples were fabricated by electron beam lithography using a negative photoresist and a single-layer lift-off process



4.22 The FDTD analysis of fields around nanoslits. (a) Simulated horizontal electric field around a 500-nm width at 0.1 THz. (b) Horizontal electric field around a 70-nm width. (c) Vertical electric field around the 70-nm width. (d) Simulated magnetic field around the 70-nm width. (e) Cross-sectional plot of the horizontal electric and magnetic fields at the exit side. (f) Time-averaged Poynting vector component  $\langle S_z \rangle$  (adapted from Reference 63).

(Fig. 4.23b). Shown in Fig. 4.23c and d are normalized amplitude spectra for two periods of 100  $\mu\text{m}$  and 30  $\mu\text{m}$ . For the 30  $\mu\text{m}$  period sample, the normalized amplitude increased to over 90% at the resonance with the hole coverage ratio of only 0.6%. The field enhancement was therefore over 150, calculated by the Kirchhoff integral formalism. Increasing the period to 100  $\mu\text{m}$ , increased the field enhancement only slightly, suggesting that the



4.23 (a) Schematic of an array of rectangular holes. (b) THz nanoantennas are fabricated by electron beam lithography using negative type of photoresist patterning. (c) Normalized transmitted amplitude through an array of nanoantennas with  $l = 100 \mu\text{m}$ ,  $w = 200 \text{ nm}$ , and  $d_x = 100 \mu\text{m}$  and  $d_y = 110 \mu\text{m}$ . (d) The same as (c) except  $d_x = 30 \mu\text{m}$ . Inset displays SEM images of the samples. (adapted from Reference 55).

antenna cross-section of each slot antenna on Si substrate was about  $100 \mu\text{m}$  by  $30 \mu\text{m}$ .

## 4.5 Conclusions

We have investigated how light emerges from holes with dimensions much smaller than the wavelength of the incident light in the THz frequency regime. THz near-field images directly show that subwavelength holes in metal film have salient features such as highly enhanced electromagnetic fields near the edges for strongly asymmetric apertures. In addition, near-field enhancement can be estimated by measuring only the far-field transmission, using the Kirchhoff formalism. This is particularly useful for nano-width apertures accompanied by enormous field enhancements, where the limited spatial resolution of the near-field imaging renders direct measurement of the enhancements difficult. We have shown that the combination of near-field imaging and far-field transmission measurements provide vital insights in such new frontier problems as the sub-skin depth barrier separating THz nanoslot antennas.

## 4.6 References

1. Ambrose, W. P., Goodwin, P. M., Martin, J. C. and Keller, R. A. Single-molecule detection and photochemistry on a surface using near-field optical-excitation. *Physical Review Letters* **72**, 160–163 (1994).
2. Nie, S. M. and Emery, S. R. Probing single molecules and single nanoparticles by surface-enhanced Raman scattering. *Science* **275**, 1102–1106 (1997).
3. Kuhn, S., Hakanson, U., Rogobete, L. and Sandoghdar, V. Enhancement of single-molecule fluorescence using a gold nanoparticle as an optical nanoantenna. *Physical Review Letters* **97**, doi:10.1103/PhysRevLett.97.017402 (2006).
4. Novotny, L., Anger, P. and Bharadwaj, P. Enhancement and quenching of single-molecule fluorescence. *Physical Review Letters* **96**, doi:10.1103/PhysRevLett.96.113002 (2006).
5. Vanden Bout, D. A., Kerimo, J., Higgins, D. A. and Barbara, P. F. Near-field optical studies of thin-film mesostructured organic materials. *Accounts of Chemical Research* **30**, 204–212, doi:10.1021/ar960274k (1997).
6. Betzig, E. and Trautman, J. K. Near-field optics: microscopy, spectroscopy, and surface modification beyond the diffraction limit. *Science* **257**, 189–195, doi:10.1126/science.257.5067.189 (1992).
7. Keilmann, F. FIR microscopy. *Infrared Physics and Technology* **36**, 217–224, doi:10.1016/1350-4495(94)00066-t (1995).
8. Ash, E. A. and Nicholls, G. Super-resolution aperture scanning microscope. *Nature* **237**, 510–512 (1972).
9. Mitrofanov, O., Brener, I., Harel, R., Wynn, J. D., Pfeiffer, L. N., West, K. W. and Federici, J. Terahertz near-field microscopy based on a collection mode detector. *Applied Physics Letters* **77**, 3496–3498 (2000).
10. Lee, M., Hsu, J.W.P., Pfeiffer, L.N., West, K.W., Wynn, J.D. and Federici, J.F. Terahertz pulse propagation through small apertures. *Applied Physics Letters* **79**, 907–909 (2001).
11. Nguyen, T. D., Vardeny, Z. V. and Nahata, A. Concentration of terahertz radiation through a conically tapered aperture. *Optics Express*, **18**, 25441–25448 (2010).
12. Zhan, H., Mendis, R. and Mittleman, D. M. Superfocusing terahertz waves below  $\lambda/250$  using plasmonic parallel-plate waveguides. *Optics Express* **18**, 9643–9650 (2010).
13. Chen, Q., Jiang, Z. P., Xu, G. X. and Zhang, X. C. Near-field terahertz imaging with a dynamic aperture. *Optics Letters* **25**, 1122–1124 (2000).
14. Mittleman, D. M., Jacobsen, R. H. and Nuss, M. C. T-ray imaging. *IEEE Journal of Selected Topics in Quantum Electronics* **2**, 679–692 (1996).
15. Hunsche, S., Koch, M., Brener, I. and Nuss, M. C. THz near-field imaging. *Optics Communications* **150**, 22–26, doi: 10.1016/s0030-4018(98)00044-3 (1998).
16. Hillenbrand, R., Taubner, T. and Keilmann, F. Phonon-enhanced light-matter interaction at the nanometre scale. *Nature* **418**, 159–162 (2002).
17. Knoll, B. and Keilmann, F. Near-field probing of vibrational absorption for chemical microscopy. *Nature* **399**, 134–137 (1999).
18. Wang, K. L., Mittleman, D. M., van der Valk, N. C. J. and Planken, P. C. M. Antenna effects in terahertz apertureless near-field optical microscopy. *Applied Physics Letters* **85**, 2715–2717, doi:10.1063/1.1797554 (2004).

19. van der Valk, N. C. J. and Planken, P. C. M. Electro-optic detection of subwavelength terahertz spot sizes in the near field of a metal tip. *Applied Physics Letters* **81**, 1558–1560, doi:10.1063/1.1503404 (2002).
20. Hillenbrand, R., Schnell, M., Garcia-Etxarri, A., Alkorta, J. and Aizpurua, J. Phase-resolved mapping of the near-field vector and polarization state in nanoscale antenna gaps. *Nano Letters* **10**, 3524–3528, doi:10.1021/nl101693a (2010).
21. Schnell, M., García-Etxarri, A., Huber, A. J., Crozier, K., Aizpurua, J., and Hillenbrand, R. Controlling the near-field oscillations of loaded plasmonic nanoantennas. *Nature Photonics* **3**, 287–291, doi:http://www.nature.com/nphoton/journal/v3/n5/supinfo/nphoton.2009.46\_S1.html (2009).
22. Bethe, H. A. Theory of diffraction by small holes. *Physical Review* **66**, 163 (1944).
23. Adam, A. J. L., Brok, J. M., Seo, M. A., Ahn, K. J., Kim, D. S., Kang, J. H., Park, Q. H., Nagel, M. and Planken, P. C. M. Advanced terahertz electric near-field measurements at sub-wavelength diameter metallic apertures. *Opt. Express* **16**, 7407–7417 (2008).
24. Knab, J. R., Adam, A. J. L., Nagel, M., Shaner, E., Seo, M. A., Kim, D. S. and Planken, P. C. M. Terahertz near-field vectorial imaging of subwavelength apertures and aperture arrays. *Optics Express* **17**, 15072–15086 (2009).
25. Adam, A. J. L., Guestin, L., Knab, J. R., Nagel, M. and Planken, P. C. M. Influence of the dielectric substrate on the terahertz electric near-field of a hole in a metal. *Optics Express* **17**, 17412–17425 (2009).
26. Planken, P. C. M., Nienhuys, H.-K., Bakker, H. J. and Wenckebach, T. Measurement and calculation of the orientation dependence of terahertz pulse detection in ZnTe. *Journal of the Optical Society of America B* **18**, 313–317 (2001).
27. van der Valk, N. C. J., Wenckebach, T. and Planken, P. C. M. Full mathematical description of electro-optic detection in optically isotropic crystals. *Journal of the Optical Society of America B* **21**, 622–631 (2004).
28. Seo, M. A., Adam, A. J. L., Kang, J. H., Lee, J. W., Jeoung, S. C., Park, Q. H., Planken, P. C. M. and Kim, D. S. Fourier-transform terahertz near-field imaging of one-dimensional slit arrays: mapping of electric-field-, magnetic-field-, and Poynting vectors. *Optics Express* **15**, 11781–11789 (2007).
29. Walther, M., Bitzer, A. and Ortner, A. Terahertz near-field microscopy with subwavelength spatial resolution based on photoconductive antennas. *Applied Optics* **49**, E1–E6 (2010).
30. Bitzer, A., Ortner, A., Merbold, H., Feurer, T. and Walther, M. Terahertz near-field microscopy of complementary planar metamaterials: Babinet's principle. *Optics Express* **19**, 2537–2545 (2011).
31. Olmon, R. L., Rang, M., Krenz, P. M., Lail, B. A., Saraf, L. V., Boreman, G. D. and Raschke, M. B. Determination of electric-field, magnetic-field, and electric-current distributions of infrared optical antennas: a near-field optical vector network analyzer. *Physical Review Letters* **105**, 167403 (2010).
32. Bitzer, A. and Walther, M. Terahertz near-field imaging of metallic subwavelength holes and hole arrays. *Applied Physics Letters* **92**, doi:10.1063/1.2936303 (2008).
33. Roberts, A. Electromagnetic theory of diffraction by a circular aperture in a thick, perfectly conducting screen. *Journal of the optical society of America A* **4**, 1970–1983 (1987).

34. Garcia-Vidal, F. J., Moreno, Esteban, Porto, J. A. and Martin-Moreno, L. Transmission of light through a single rectangular hole. *Physical Review Letters* **95**, 103901 (2005).
35. Webb, K. J. and Li, J. Analysis of transmission through small apertures in conducting films. *Physical Review B* **73**, doi:10.1103/PhysRevB.73.033401 (2006).
36. de Abajo, F. J. G. I. Light transmission through a single cylindrical hole in a metallic film. *Opt Express* **10**, 1475–1484 (2002).
37. Lezec, H. J., Degiron, A., Devaux, E., Linke, R. A., Martin-Moreno, L., Garcia-Vidal, F. J. and Ebbesen, T. W. Beaming light from a subwavelength aperture. *Science* **297**, 820–822, doi:10.1126/science.1071895 (2002).
38. Ebbesen, T. W., Lezec, H. J., Ghaemi, H. F., Thio, T. and Wolff, P. A. Extraordinary optical transmission through sub-wavelength hole arrays. *Nature* **391**, 667–669 (1998).
39. Genet, C. and Ebbesen, T. W. Light in tiny holes. *Nature* **445**, 39–46 (2007).
40. Garcia-Vidal, F. J., Martin-Moreno, M., Ebbesen, T. W. and Kuipers, L. Light passing through subwavelength apertures. *Reviews of Modern Physics* **82**, 729–787, doi:citeulike-article-id:6969700 (2010).
41. Pendry, J. B., Martín-Moreno, L. and Garcia-Vidal, F. J. Mimicking surface plasmons with structured surfaces. *Science* **305**, 847–848 (2004).
42. Degiron, A., Lezec, H. J., Yamamoto, N. and Ebbesen, T. W. Optical transmission properties of a single subwavelength aperture in a real metal. *Optics Communications* **239**, 61–66, doi:DOI: 10.1016/j.optcom.2004.05.058 (2004).
43. Cao, H. and Nahata, A. Resonantly enhanced transmission of terahertz radiation through a periodic array of subwavelength apertures. *Optics Express* **12**, 1004–1010 (2004).
44. Koerkamp, K. J. K., Enoch, S., Segerink, F. B., van Hulst, N. F. and Kuipers, L. Strong influence of hole shape on extraordinary transmission through periodic arrays of subwavelength holes. *Physical Review Letters* **92**, 183901 (2004).
45. Gordon, R., Brolo, A. G., McKinnon, A., Rajora, A., Leathem, B. and Kavanagh, K. L. Strong polarization in the optical transmission through elliptical nanohole arrays. *Physical Review Letters* **92**, 037401 (2004).
46. Degiron, A. and Ebbesen, T. W. The role of localized surface plasmon modes in the enhanced transmission of periodic subwavelength apertures. *Journal of Optics A: Pure and Applied Optics* **7**, S90 (2005).
47. Ruan, Z. and Qiu, M. Enhanced transmission through periodic arrays of subwavelength holes: the role of localized waveguide resonances. *Physical Review Letters* **96**, 233901 (2006).
48. Lee, J. W., Seo, M. A., Kang, D. H., Khim, K. S., Jeoung, S. C. and Kim, D. S. Terahertz electromagnetic wave transmission through random arrays of single rectangular holes and slits in thin metallic sheets. *Physical Review Letters* **99**, 137401 (2007).
49. Lee, J. W., Seo, M. A., Park, D. J. and Kim, D. S., Jeoung, S. C., Lienau, Ch., Park, Q. H. and Planken, P. C. M. Shape resonance omni-directional terahertz filters with near-unity transmittance. *Opt. Express* **14**, 1253–1259 (2006).
50. Bouwkamp, C. J. Diffraction theory. *Reports on Progress in Physics* **17**, 35 (1954).
51. Born, M. and Wolf, E. *Principles of Optics*. (Cambridge University Press, 1999).
52. Jackson, J. D. *Classical Electrodynamics*. (John Wiley & Sons, Inc., 2001).

53. Kihm, H. W., Koo, S. M., Kim, Q. H., Bao, K., Kihm, J. E., Bak, W. S., Eah, S. H., Lienau, C., Kim, H., Nordlander, P., Halas, N. J., Park, N. K. and Kim, D.-S. Bethe-hole polarization analyser for the magnetic vector of light. *Nat Commun* **2**, 451, doi:[http://www.nature.com/ncomms/journal/v2/n8/supinfo/10.1038-ncomms1430-unlocked-60x70\\_S1.html](http://www.nature.com/ncomms/journal/v2/n8/supinfo/10.1038-ncomms1430-unlocked-60x70_S1.html) (2011).
54. Seo, M. A., Adam, A. J. L., Kang, J. H., Lee, J. W., Ahn, K. J., Park, Q. H., Planken, P. C. M. and Kim, D. S. Near field imaging of terahertz focusing onto rectangular apertures. *Optics Express* **16**, 20484–20489 (2008).
55. Park, H. R., Park, Y. M., Kim, H. S., Kyoung, J. S., Seo, M. A., Park, D. J., Ahn, Y. H., Ahn, K. J. and Kim, D. S. Terahertz nanoresonators: giant field enhancement and ultrabroadband performance. *Applied Physics Letters* **96**, 121106–121103, doi:10.1063/1.3368690 (2010).
56. Bahk, Y. M., Park, H. R., Ahn, K. J., Kim, H. S., Ahn, Y. H., Kim, D.-S., Bravo-Abad, J., Martín-Moreno, L. and García-Vidal, F. J. Anomalous band formation in arrays of terahertz nanoresonators. *Physical Review Letters* **106**, 013902 (2011).
57. Seo, M., Kyoung, J., Park, H., Koo, S., Kim, H. S., Bernien, H., Kim, B. J., Choe, J. H., Ahn, Y. H., Kim, H. T., Park, N., Park, Q. H., Ahn, K. and Kim, D. S. Active Terahertz nanoantennas based on VO<sub>2</sub> phase transition. *Nano Lett* **10**, 2064–2068, doi:10.1021/nl1002153 (2010).
58. Kyoung, J., Seo, M., Park, H., Koo, S., Kim, H. S., Park, Y., Kim, B. J., Ahn, K., Park, N., Kim, H. T. and Kim, D. S. Giant nonlinear response of terahertz nanoresonators on VO<sub>2</sub> thin film. *Optics Express* **18**, 16452–16459 (2010).
59. Choi, S. B., Kyoung, J. S., Kim, H. S., Park, H. R., Park, D. J., Kim, B.-J., Ahn, Y. H., Rotermund, F., Kim, H.-T., Ahn, K. J. and Kim, D. S. Nanopattern enabled terahertz all-optical switching on vanadium dioxide thin film. *Applied Physics Letters* **98**, 071105–071103, doi:10.1063/1.3553504 (2011).
60. Jeong, Y.-G., Bernien, H., Kyoung, J. S., Park, H. R., Kim, H. S., Choi, J. W., Kim, B. J., Kim, H. T., Ahn, K. J. and Kim, D. S. Electrical control of terahertz nano antennas on VO<sub>2</sub> thin film. *Optics Express* **19**, 21211–21215 (2011).
61. Park, H.-R., Bahk, Y. M., Ahn, K. J., Park, Q. H., Kim, D. S., Martín-Moreno, L., García-Vidal, F. J. and Bravo-Abad, J. Controlling terahertz radiation with nanoscale metal barriers embedded in nano slot antennas. *ACS Nano* **5**, 8340–8345, doi:10.1021/nn2031885 (2011).
62. Kyoung, J. S., Seo, M. A., Park, H. R., Ahn, K. J. and Kim, D. S. Far field detection of terahertz near field enhancement of sub-wavelength slits using Kirchhoff integral formalism. *Optics Communications* **283**, 4907–4910, doi: 10.1016/j.optcom.2010.08.008 (2010).
63. Seo, M. A., Park, H. R., Koo, S. M., Park, D. J., Kang, J. H., Suwal, O. K., Choi, S. S., Planken, P. C. M., Park, G. S., Park, N. K., Park, Q. H. and Kim, D. S. Terahertz field enhancement by a metallic nano slit operating beyond the skin-depth limit. *Nat Photon* **3**, 152–156 (2009).
64. Park, H. R., Koo, S. M., Suwal, O. K., Park, Y. M., Kyoung, J. S., Seo, M. A., Choi, S. S., Park, N. K., Kim, D. S. and Ahn, K. J. Resonance behavior of single ultrathin slot antennas on finite dielectric substrates in terahertz regime. *Applied Physics Letters* **96**, 211109–211103, doi:10.1063/1.3437091 (2010).